IEEE Journal of Microwaves

Received 14 March 2024; accepted 21 April 2024. Date of publication 8 May 2024;
date of current version 12 July 2024.

Digital Object Identifier 10.1109/JMW.2024.3393120

Constellation Estimation, Coherent Signal Processing, and Multiperspective Imaging in an Uncoupled Bistatic Cooperative Radar Network

PATRICK FENSKE (Graduate Student Member, IEEE), TOBIAS KOEGEL (Graduate Student Member, IEEE), ROGHAYEH GHASEMI (Graduate Student Member, IEEE), AND MARTIN VOSSIEK (Fellow, IEEE)

(Regular Paper)

Institute of Microwaves and Photonics, Friedrich-Alexander-Universität Erlangen-Nürnberg, 91058 Erlangen, Germany

CORRESPONDING AUTHOR: Patrick Fenske (e-mail: patrick.fenske@fau.de).

This work was supported in part by German Research Foundation (DFG) under Grant GRK 2680 – Project-ID 437847244 and in part by the German Federal Ministry of Education and Research (BMBF) in the framework of the 6G research hub 6GEM under Grant 16KISK044.

ABSTRACT Cooperative radar networks are a promising technology in various areas, such as vehicle-to-infrastructure networks for automotive radar and radar remote sensing with UAVs. The use of widely distributed radar networks enables the detection of targets with complex scattering characteristics, as their coherent bistatic images are superior for forward scattering, and each monostatic image illuminates a scene from a different perspective. This work introduces a signal processing scheme that addresses two main challenges in this area: the coherent signal processing of uncoupled radar nodes and the self-localization of the nodes for radar image combination. A comprehensive signal model that incorporates time, frequency and phase incoherency is introduced. Based on this, an algorithm for constellation estimation, synchronization up to the carrier phase level, and multiperspective imaging is developed. The proposed approach is experimentally verified using commercially available 77 GHz single-input/multiple-output radar nodes. The measurements for different radar constellations and various target scenes show a self-localization accuracy below 6 cm in range and below 2.5° for the incident angles. The resulting images of various scenes clearly indicate an information gain compared to single monostatic images due to the combination of bistatic and multiperspective monostatic images.

INDEX TERMS Bistatic radar, chirp sequence modulation, cooperative radar networks, FMCW, localization, millimeter-wave radar, multiperspective imaging, radar networks, synchronization.

I. INTRODUCTION

Distributed cooperative radar networks are seen as an emerging technology in several technical areas. In the automotive world, where most vehicles are equipped with multiple radar sensors, a trend is towards combining single sensors nodes into a multistatic system and applying coherent processing [1], [2], [3], [4]. Ideas go even further, shifting from fixed-mounted radar nodes on a common frame, such as an automobile or unmanned aerial vehicle (UAV), to individually moving, uncoupled radar nodes. For example, [5] suggests the integration of radar sensors into the 6G infrastructure, with several base stations and radio units in a cloud radio access network building an ad hoc multistatic radar system, thus promising high spatial resolution, improved detection, and precise tracking. Further applications of distributed radar networks are presented in [6] and [7]. The former promotes the idea of using UAV-mounted radar networks for aerial surveillance, while the latter proposes UAV-based radar networks for radar remote sensing applications.

The spatial diversity of distributed multistatic radar networks can significantly improve the radar image resolution [8], [9], enabling more precise target position and velocity

estimates [10]. Another benefit is improved target detection performance in the presence of clutter, as demonstrated in [11]. Furthermore, depending on the target material and geometry, different scattering characteristics of a radar target are possible [12]. Stealth targets, for example, can be resolved better by bistatic systems [13], [14], [15]. Hence, combining monostatic and bistatic signals into a multiperspective radar image can better handle different targets with varying angle-dependent radar cross-sections (RCSs).

Nevertheless, the coherent processing of bistatic radar signals in an uncoupled multistatic scenario comes with challenging tasks. The two radar nodes that form a bistatic constellation need to be synchronized in time, frequency and carrier phase for coherent operation [16]. Moreover, for bistatic image generation and multistatic image combination, the relative positions of all transmitting (TX) and receiving (RX) antennas need to be precisely known to improve image quality [17].

Several previous works have dealt with signal processing challenges in loosely coupled or uncoupled bi- and multistatic radar systems. In [18], a synchronization and processing scheme for quasi-coherent range and velocity estimation in a wireless locating system between two radar nodes is introduced. This approach achieves performance comparable to that of a coherent monostatic radar system. The single-input/single-output (SISO) nodes employ a single Tx-Rx antenna, which facilitates processing due to a reciprocal channel assumption but can measure only distances and radial velocities between the two units. Another approach with similar processing steps is proposed in [19] and [2]. Here, the two units are not supposed to locate each other but are mounted on the same fixture to span a large antenna aperture for automotive radar imaging. This significantly improves the spatial resolution and enables the separation of nearby targets. The radar nodes are coupled by an 80 MHz reference clock and share a common trigger signal, which simplifies time and phase synchronization. This coarse pre-synchronization with low frequency clock and trigger signals is suitable as long as both radar units are installed on the same platform — for example, on a car. However, if the two radar units are installed on different platforms, they need to be completely uncoupled. In this case, all synchronization tasks need to be performed wirelessly, which poses considerable, challenges especially if phase coherency or even phase noise coherency is intended [19]. The works presented in [20], [21], and [3] introduce coherent processing schemes for bistatic frequency-modulated continuous-wave (FMCW) chirp sequence (CS) signals in an uncoupled radar network. Phase coherency is achieved there, but less attention is paid to phase noise effects. In the presence of strong phase noise, which is the case for bistatic radars with independent local oscillators (LOs), the noise skirt can be superimposed, concealing targets with low RCSs [22]. An uncoupled bistatic radar network with phase noise compensation is introduced in [23], achieving very good compensation performance in a SISO setup with antennas placed close together. However, a drawback of all these approaches is that they are suitable only for wireless locating or perform imaging in a bistatic constellation with the radar nodes fixed on a common frame and are thus not capable of multiperspective imaging.

The use of repeater nodes to form a multistatic network is introduced in [24] and [4]. This approach relaxes the synchronization requirements, as all radar signals are generated by the same node and are forwarded by a repeater node. On the other hand, this adds more noise to the bistatic signal and is not applicable to scenarios with strong multipath reflections because the repeater will cause significant increase in the number of multipath components. A concept for widely distributed multistatic and uncoupled radar networks is presented in [25], which uses an additional degree of freedom per target in the measurement for synchronization and self-localization, making success dependent on the number of targets present in a scene. This concept lacks verification through measurements, but simulations indicate a synchronization accuracy in the nanosecond range and a localization root mean square error of 0.81 m.

The contribution of this paper to the field of distributed radar networks is the first experimentally verified concept for simultaneous self-localization and imaging of uncoupled and independently moving FMCW radar nodes in a bistatic constellation. The great advantage of the proposed approach is that the same signals are used for relative pose estimation, digital synchronization, and radar imaging. Localization and synchronization are performed using bistatic line-of-sight (LoS) signals. After compensating for signal disturbances due to timing and phase errors, and with the precise knowledge of all bistatic antenna positions, bistatic radar images are produced using a back-projection algorithm. Additionally, the information from each monostatic radar signal can be used to enhance the overall image quality. Our approach can be implemented using conventional single-input/multiple-output (SIMO) radars.

The rest of the paper is organized as follows: In Section II, an extensive signal model for the proposed bistatic radar system is presented, which incorporates time and frequency deviations between the two radars, uncorrelated carrier phases, and phase noise. This model serves as the basis for the simulation framework that underlies the consecutive signal processing steps. Section III describes the estimation procedure for the radar network's relative 2D pose. Section IV presents the necessary steps for synchronizing the bistatic signals. Section V describes how the bistatic signals are used to create bistatic images of a scene and how bistatic and monostatic images are combined to provide a general view of the scene. Section VI demonstrates the concept's capabilities based on real radar measurements.

II. SYSTEM AND SIGNAL MODEL

In the proposed bistatic network, each node consists of a SIMO FMCW radar with one TX antenna and N_{rx} RX antennas. Each radar is equipped with its own reference oscillator, yielding independent local time bases, an unknown carrier

phase relationship between the two LOs, and uncorrelated phase noise. To deal with the given conditions, a comprehensive signal model is developed. Despite using monostatic and bistatic signals for image processing, only the bistatic model is explained in detail herein. Critical aspects, such as synchronization errors and uncorrelated phase noise, can be ignored in the monostatic case.

A. TIME MODEL

First, the independent local time bases are investigated. A constant time drift model is used to express the local times in each unit (with index i) relative to a common global time

$$t_i(t) = \left(1 + \delta_{\mathrm{t},i}\right) t + \Delta\tau_{0,i} \quad \text{with} \quad i \in \{1, 2\}, \tag{1}$$

where $\delta_{\mathrm{t},i}$ is the time drift that arises from the deviation between the two oscillator reference frequencies f^i_{ref} and the nominal frequency f_{ref} and is calculated as $\delta_{\mathrm{t},i} = \frac{f^i_{\mathrm{ref}} - f_{\mathrm{ref}}}{f_{\mathrm{ref}}}$. The initial time offset at the start of a chirp sequence to a common, arbitrary global time origin is referred to as $\Delta\tau_{0,i}$ and depends on the quality of time pre-synchronization between the two units. The bistatic radar signal model is simplified through some assumptions about the symmetry of the errors with negligible consequences for the processing results [18]. The global time origin is centered between the start times of the two radars $\Delta\tau_{0,1} = \frac{\Delta\tau_0}{2} = -\Delta\tau_{0,2}$. Similarly, it is assumed that both reference frequencies are symmetrically offset around the nominal frequency $\delta_{\mathrm{t},1} = \frac{\delta_{\mathrm{t}}}{2} = -\delta_{\mathrm{t},2}$. To define the requirements for time pre-synchronization and the reference oscillator quality in terms of frequency deviation in parts per million, the beat frequency offset induced by the timing error, as illustrated in Fig. 1, needs to be considered. The beat frequency of the n_{ch}-th chirp in a FMCW-CS signal of N_{ch} chirps depends mainly on the time of flight (ToF) τ_{ToF} and the time offset at the chirp start $\Delta\tau_{n_{\mathrm{ch}}}$. The latter can be calculated by

$$\Delta\tau_{n_{\mathrm{ch}}} = t_2\left(n_{\mathrm{ch}} T_{\mathrm{rep}}\right) - t_1\left(n_{\mathrm{ch}} T_{\mathrm{rep}}\right) = -n_{\mathrm{ch}}\delta_{\mathrm{t}} T_{\mathrm{rep}} - \Delta\tau_0, \tag{2}$$

where T_{rep} is the chirp repetition time of the sequence. The limitation of the maximum time drift and offset is given by the Nyquist sampling criterion of the bistatic beat signals due to the radar's sampling frequency f_{s}:

$$\left|-\mu\left(\tau_{\mathrm{ToF}} \pm \Delta\tau_{n_{\mathrm{ch}}}\right)\right| \leq \frac{f_{\mathrm{s}}}{2} \quad \forall\, n_{\mathrm{ch}} \in \{0, \ldots, N_{\mathrm{ch}} - 1\}, \tag{3}$$

where $\mu = \frac{B}{T_{\mathrm{ch}}}$ is the chirp rate. The sign of the respective time offset in (3) depends on which radar is transmitting and which is receiving. The requirements are individually set by the system's parameters, which are the sampling frequency, the maximum detectable range, the chirp slope, and the number of chirps during one sequence. An exemplary test of this condition for a given system parameter set is shown in Fig. 2. If the criterion from (3) is not met, either the system's parameters must be readjusted, or the pre-synchronization has to be improved. Otherwise, the resulting beat signals cannot be measured for all chirps in the sequence because some may not fulfill the Nyquist criterion.

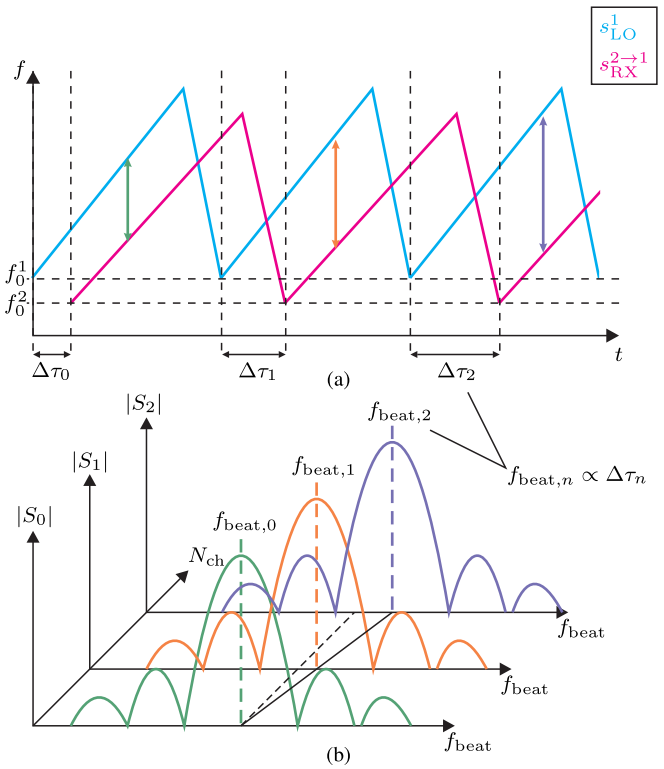

FIGURE 1. Model of consecutive bistatic RX and LO chirps in one radar node in (a) a time–frequency representation and (b) after fast time Fourier transform. A linear increasing timing error is assumed to emphasize the influence of time and frequency errors on the beat signal.

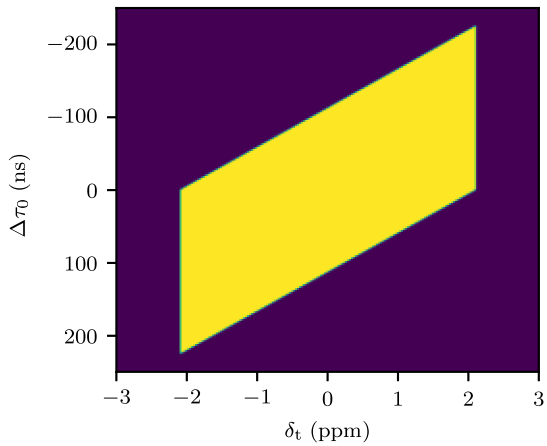

FIGURE 2. Evaluation of the synchronization condition from (3) with the following system parameters: $f_{\mathrm{s}} = 2$ MHz, $B = 1.5$ GHz, $T_{\mathrm{ch}} = 512$ µs, $T_{\mathrm{rep}} = 1024$ µs, $N_{\mathrm{ch}} = 128$, and $d_{\mathrm{max}} = 50$ m. The yellow area indicates that the requirement is fulfilled.

B. PHASE NOISE

After examining the deterministic timing errors, the influence of the LOs' phase noise on the bistatic signals is investigated. The modelling approach presented in [26] is used to simulate a realistic phase noise behavior with the power spectral density

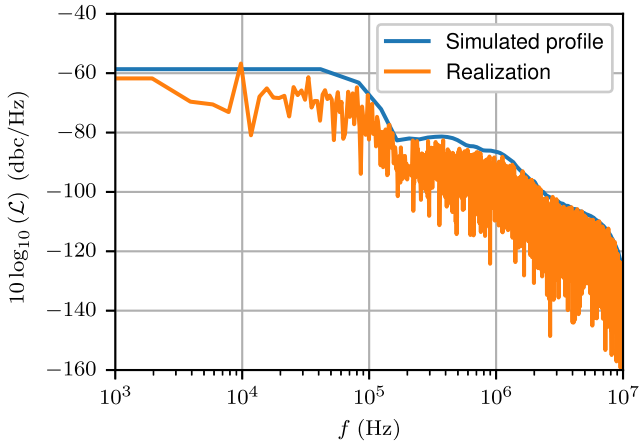

FIGURE 3. PSD profile that serves as the basis for simulations and calculated PSD from one noise realization.

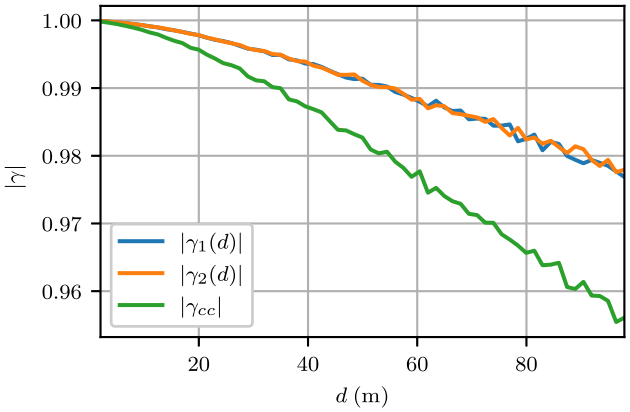

FIGURE 4. Correlation between the transmitter phase noise in stations 1 and 2 (γ_1 and γ_2, respectively) and its delayed version. Cross-correlation (γ_{cc}) between the phase noise of the beat signal in radar 1 and the complex conjugate beat signal in station 2.

shown in Fig. 3. For each radar unit, a separate sample function is drawn, yielding the phase noise signal for the respective LO which is calculated as

$$s_{\mathrm{TX,pn},1/2}(t) = \mathrm{e}^{\mathrm{j}\phi_{\mathrm{pn},1/2}(t)}. \tag{4}$$

In the bistatic beat signal, the delayed phase noise of the transmitter is multiplied with the complex conjugate of the receiver's phase noise. This can be mathematically expressed as

$$s_{\mathrm{pn}}^{2\to1}(t) = \mathrm{e}^{\mathrm{j}(\phi_{\mathrm{pn},2}(t-\tau)-\phi_{\mathrm{pn},1}(t))} \tag{5}$$

$$s_{\mathrm{pn}}^{1\to2}(t) = \mathrm{e}^{\mathrm{j}(\phi_{\mathrm{pn},1}(t-\tau)-\phi_{\mathrm{pn},2}(t))}, \tag{6}$$

where τ is the ToF, which is assumed to be equal in both directions. The phase noise components in both bistatic beat signals appear similarly apart from the ToF shift of the respective transmitting station. To evaluate the influence of the time shift on the correlation, the correlation function described in [27] is used:

$$\gamma_{12}(\tau) = \frac{\langle V_1(t+\tau), V_2^*(t)\rangle}{\sqrt{\langle V_1(t), V_1^*(t)\rangle \cdot \langle V_2(t), V_2^*(t)\rangle}}, \tag{7}$$

where $\langle\cdot,\cdot\rangle$ indicates the inner product. The results are shown in Fig. 4. The time shift is converted to an equivalent bistatic radar distance $d = \tau/c_0$. As shown in Fig. 4, a good correlation is preserved, even for a distance of 100 m. Another figure of merit for assessing the influence of phase noise decorrelation is the comparison of the noise-induced errors in the frequency and phase estimates at both bistatic beat signals given a single target at various distances. Fig. 5 shows that the errors of both estimates are strongly correlated and the residual error due to range decorrelation is negligible. Consequently, the uncorrelated phase noise can be simplified as:

$$\mathrm{e}^{\mathrm{j}(\phi_{\mathrm{pn},2}(t-\tau)-\phi_{\mathrm{pn},1}(t))} \approx \mathrm{e}^{\mathrm{j}(\phi_{\mathrm{pn},2}(t)-\phi_{\mathrm{pn},1}(t))}, \tag{8}$$

$$\mathrm{e}^{\mathrm{j}(\phi_{\mathrm{pn},1}(t-\tau)-\phi_{\mathrm{pn},2}(t))} \approx \mathrm{e}^{\mathrm{j}(\phi_{\mathrm{pn},1}(t)-\phi_{\mathrm{pn},2}(t))}. \tag{9}$$

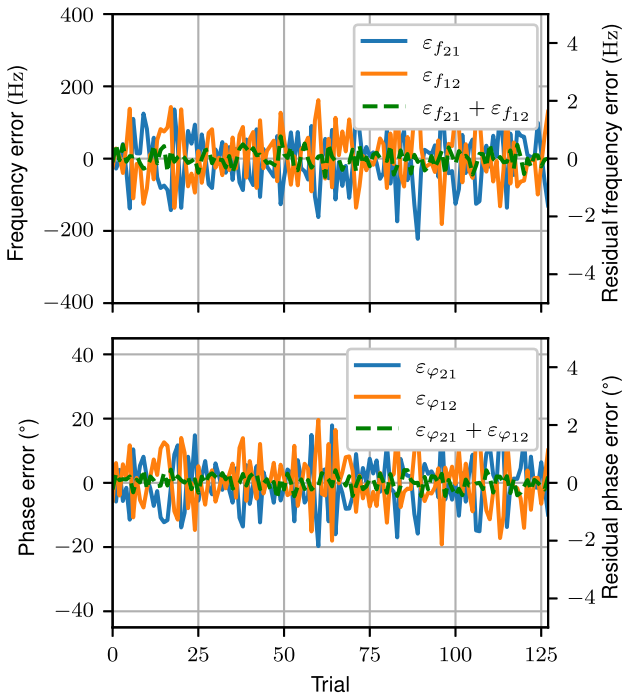

FIGURE 5. Monte Carlo simulation (128 trials) of the frequency and phase errors due to phase noise in the bistatic signals with a single target. The target's range is sampled according to $d \sim \mathcal{N}(\mu = 20\,\mathrm{m}, \sigma = 5\,\mathrm{m})$ for each trial. The dashed green line indicates the residual error due to range decorrelation and refers to the right y-axis.

This step can also be derived mathematically by a first-order Taylor expansion of the delayed phase noise term at time t, exemplarily shown for the first radar's phase noise

$$\phi_{\mathrm{pn},1}(t-\tau) \approx \phi_{\mathrm{pn},1}(t) + \dot{\phi}_{\mathrm{pn},1}(t)\cdot\tau \approx \phi_{\mathrm{pn},1}(t), \tag{10}$$

where the second assumption is valid if the change in the phase disturbance $\dot{\phi}_{\mathrm{pn},1}(t)$ is considerably smaller than $2\pi/\tau$, yielding $\dot{\phi}_{\mathrm{pn},1}(t)\cdot\tau \ll \pi$. Hence, the phase noise signal

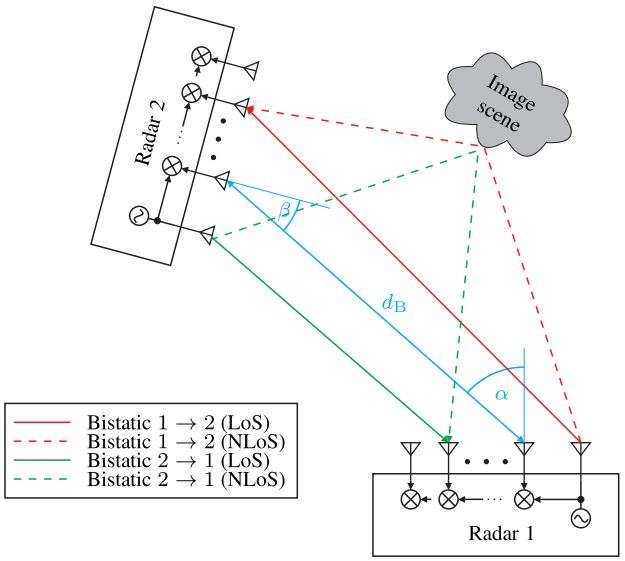

FIGURE 6. Sketch of the bistatic SIMO radar setup. The baseline length d_B and the angles α and β fully describe the radars' positions relative to each other. The bistatic signal path in both directions consists of one LoS path and several non-LoS (NLoS) paths, depending on the number of scatterers in the image scene.

model simplifies as

$$s_{\mathrm{pn}}^{2\to1}(t) = \mathrm{e}^{\mathrm{j}\overbrace{\left(\phi_{\mathrm{pn},2}(t)-\phi_{\mathrm{pn},1}(t)\right)}^{=\Delta\phi_{\mathrm{pn}}(t)}} = s_{\mathrm{pn}}^{1\to2^*}(t), \tag{11}$$

where $(\cdot)^*$ denotes the complex conjugate.

C. GEOMETRY

To complete the signal model, the mathematical descriptions of the relative antenna positions in the bistatic constellaton are derived. The TX antenna of the first radar is located at $\vec{p}_{\mathrm{TX},1}$, and the position of the radar's n_{A}-th RX antenna is $\vec{p}_{\mathrm{RX},1,n_{\mathrm{A}}}$. The 2D positions of the second radar's antennas are calculated using the parameters described in Fig. 6. The angles α and β are the inclinations of the LoS signals relative to the looking directions of the first and second radars, respectively. The baseline length d_{B} is defined as the distance between each first RX antenna. The application of rotation by the angle $\gamma = \alpha - \beta - \pi$ and a subsequent translation by the baseline vector $\vec{p}_{\mathrm{B}} = (-d_{\mathrm{B}}\sin\alpha \quad d_{\mathrm{B}}\cos\alpha)^{\mathrm{T}}$ yield the antenna positions of the second radar as

$$\vec{p}_{\mathrm{TX},2} = \begin{pmatrix}\cos\gamma & -\sin\gamma\\ \sin\gamma & \cos\gamma\end{pmatrix}\vec{p}_{\mathrm{TX},1} + \vec{p}_{\mathrm{B}}, \tag{12}$$

$$\vec{p}_{\mathrm{RX},2,n_{\mathrm{A}}} = \begin{pmatrix}\cos\gamma & -\sin\gamma\\ \sin\gamma & \cos\gamma\end{pmatrix}\vec{p}_{\mathrm{RX},1,n_{\mathrm{A}}} + \vec{p}_{\mathrm{B}}. \tag{13}$$

The ToFs of the LoS signals are given by

$$\tau_{n_{\mathrm{A}}}^{2\to1} = \frac{\left\|\vec{p}_{\mathrm{RX},1,n_{\mathrm{A}}} - \vec{p}_{\mathrm{TX},2}\right\|}{c_0}, \tag{14}$$

$$\tau_{n_{\mathrm{A}}}^{1\to2} = \frac{\left\|\vec{p}_{\mathrm{RX},2,n_{\mathrm{A}}} - \vec{p}_{\mathrm{TX},1}\right\|}{c_0}, \tag{15}$$

and the delays of a target at point $\vec{p}_\ell$ in the image scene are

$$\tau_{\ell,n_{\mathrm{A}}}^{2\to1} = \frac{\left\|\vec{p}_{\mathrm{RX},1,n_{\mathrm{A}}} - \vec{p}_\ell\right\| + \left\|\vec{p}_\ell - \vec{p}_{\mathrm{TX},2}\right\|}{c_0}, \tag{16}$$

$$\tau_{\ell,n_{\mathrm{A}}}^{1\to2} = \frac{\left\|\vec{p}_{\mathrm{RX},2,n_{\mathrm{A}}} - \vec{p}_\ell\right\| + \left\|\vec{p}_\ell - \vec{p}_{\mathrm{TX},1}\right\|}{c_0}, \tag{17}$$

where ℓ is the point target index in a multi-target scene.

D. BISTATIC SIGNALS

For the conventional chirp sequence approach, linear modulation is applied to the LO frequencies in both units expressed in their local times

$$f_{\mathrm{TX},i}(t_i) = f_{0,i} + \mu t_i \quad \text{with} \quad i \in \{1,2\}, \tag{18}$$

where $\mu = \frac{B}{T_{\mathrm{ch}}}$ is the chirp rate, $f_{0,i}$ is the carrier frequency of the respective unit, and B and T_{ch} are the bandwidth and chirp duration, respectively. To separate the bistatic and monostatic signals, a beat frequency–division multiplexing (FDM) scheme is applied, yielding the relationship $f_{0,2} = f_{0,1} + \Delta f$ [28]. The procedure for calculating the bistatic beat signals and simplifying them by crossing out negligible terms is described in detail in [18]. These results and the introduced models are used for the local times, the phase noise, and the ToFs to give the bistatic LoS beat signals after FDM channel separation as

$$\begin{aligned} s_{\mathrm{B,LoS},k,n_{\mathrm{A}}}^{2\to1}(t) \approx{}& A_{\mathrm{LoS},k,n_{\mathrm{A}}}^{2\to1}\cdot \\ &\exp\left\{2\pi\mathrm{j}\left[-f_{0,\mathrm{c}}\delta_{\mathrm{t}} - \mu\tau_{k,n_{\mathrm{A}}}^{2\to1} + \mu\left(\Delta\tau_0 + kT_{\mathrm{rep}}\delta_{\mathrm{t}}\right)\right]t\right. \\ &\left. - 2\pi\mathrm{j}f_0\tau_{k,n_{\mathrm{A}}}^{2\to1} + \mathrm{j}\Delta\phi_{\mathrm{pn}}(t) + \mathrm{j}\underbrace{\left(\Theta_{k,2}-\Theta_{k,1}\right)}_{=\Delta\Theta_k}\right\} \\ &\cdot\exp\left\{-2\pi\mathrm{j}\mu\delta_{\mathrm{t}}t^2\right\}, \end{aligned} \tag{19}$$

$$\begin{aligned} s_{\mathrm{B,LoS},k,n_{\mathrm{A}}}^{1\to2}(t) \approx{}& A_{\mathrm{LoS},k,n_{\mathrm{A}}}^{1\to2}\cdot \\ &\exp\left\{2\pi\mathrm{j}\left[f_{0,\mathrm{c}}\delta_{\mathrm{t}} - \mu\tau_{k,n_{\mathrm{A}}}^{1\to2} - \mu\left(\Delta\tau_0 + kT_{\mathrm{rep}}\delta_{\mathrm{t}}\right)\right]t\right. \\ &\left. - 2\pi\mathrm{j}f_0\tau_{k,n_{\mathrm{A}}}^{1\to2} - \mathrm{j}\Delta\phi_{\mathrm{pn}}(t) - \mathrm{j}\Delta\Theta_k\right\}\cdot\exp\left\{2\pi\mathrm{j}\mu\delta_{\mathrm{t}}t^2\right\}, \end{aligned} \tag{20}$$

where $f_{0,\mathrm{c}}$ is the center between the two chirp start frequencies, and $\Theta_{k,1}$ and $\Theta_{k,2}$ are the start phases of the k-th chirp for the first and second radars, respectively. This model is applied similarly to the scatterer reflections giving the combined signal models for the k-th chirp and the n_{A}-th RX channel

$$s_{\mathrm{B},k,n_{\mathrm{A}}}^{2\to1}(t) = s_{\mathrm{B,LoS},k,n_{\mathrm{A}}}^{2\to1}(t) + \sum_\ell s_{\mathrm{B},\ell,k,n_{\mathrm{A}}}^{2\to1}(t) + n_{1,k,n_{\mathrm{A}}}(t), \tag{21}$$

$$s^{1\to2}_{\mathrm{B},k,n_\mathrm{A}}(t) = s^{1\to2}_{\mathrm{B,LoS},k,n_\mathrm{A}}(t) + \sum_{\ell} s^{1\to2}_{\mathrm{B},\ell,k,n_\mathrm{A}}(t) + n_{2,k,n_\mathrm{A}}(t), \tag{22}$$

where ℓ is the index of the targets in the scene. The additive white Gaussian noise (AWGN) $n_{1/2,k,n_\mathrm{A}}(t)$ is considered uncorrelated between all RX channels and its power depends on the analog bandwidth and the receiver's noise figure.

III. CONSTELLATION ESTIMATION

The bistatic constellation is given by all TX and RX antenna positions of both radars. For common image processing, it is sufficient to know the positions of all antennas in the network relative to each other. The estimation of these positions is performed using the LoS signals. As the attenuation of the LoS signals decreases by $1/R^2$ according to free-space path loss, while the image reflections decrease proportionally to $1/R^4$ due to the radar equation [12], the strongest detected peak of the bistatic fast time fast Fourier transform (FFT) can be assumed to be an LoS peak. Therefore, a parabolic fit is applied to the FFT's maximum, and the phase is interpolated linearly to precisely detect the LoS beat frequency and the corresponding phase, which is described in detail in [29]. This yields the frequencies

$$f^{2\to1}_{\mathrm{LoS},k,n_\mathrm{A}} = -\mu\tau^{2\to1}_{0,n_\mathrm{A}} - f_\mathrm{D} - f_{0\mathrm{c}}\delta_\mathrm{t} + \mu\left(\Delta\tau_0 + kT_\mathrm{rep}\delta_\mathrm{t}\right) + \epsilon_{f,\mathrm{pn},k}, \tag{23}$$

$$f^{1\to2}_{\mathrm{LoS},k,n_\mathrm{A}} = -\mu\tau^{1\to2}_{0,n_\mathrm{A}} - f_\mathrm{D} + f_{0\mathrm{c}}\delta_\mathrm{t} - \mu\left(\Delta\tau_0 + kT_\mathrm{rep}\delta_\mathrm{t}\right) + \epsilon_{f,\mathrm{pn},k}, \tag{24}$$

where f_D is the Doppler frequency due to a constant radial velocity v_r of the second radar relative to the first. The peak phases are described by the constant velocity model as

$$\hat{\varphi}^{2\to1}_{\mathrm{LoS},k,n_\mathrm{A}} = -2\pi f_0\left[\tau^{2\to1}_{0,n_\mathrm{A}} + kT_{\mathrm{s,st}}\frac{v_\mathrm{r}}{c_0}\right] + \epsilon_{\varphi,\mathrm{pn},k} + \Delta\Theta_k \tag{25}$$

$$\hat{\varphi}^{1\to2}_{\mathrm{LoS},k,n_\mathrm{A}} = -2\pi f_0\left[\tau^{1\to2}_{0,n_\mathrm{A}} + kT_{\mathrm{s,st}}\frac{v_\mathrm{r}}{c_0}\right] - \epsilon_{\varphi,\mathrm{pn},k} - \Delta\Theta_k, \tag{26}$$

where $\epsilon_{f/\varphi,\mathrm{pn},k}$ are the phase noise-induced frequency and phase estimation errors, which are strongly correlated in both radars' measurements, as shown in Section II. The corresponding magnitudes of the fast time FFT peaks are denoted as $\hat{A}^{2\to1}_{\mathrm{LoS},k,n_\mathrm{A}}$ and $\hat{A}^{1\to2}_{\mathrm{LoS},k,n_\mathrm{A}}$.

A. INCIDENT ANGLE ESTIMATION

The same algorithm is used for estimating the angles α and β, respectively. Therefore, only the calculation of α is shown based on the measurements of the signal from radar 2 to radar 1. The complex peak phases of the bistatic RX signal in radar 1 form the measurement vector

$$\vec{x}^{2\to1}_{\mathrm{LoS},k} = \begin{bmatrix} 1 \\ A^{2\to1}_{\mathrm{LoS},k,1}/A^{2\to1}_{\mathrm{LoS},k,0}\cdot \mathrm{e}^{-2\pi\mathrm{j}f_0\left[\tau^{2\to1}_{0,1}-\tau^{2\to1}_{0,0}\right]} \\ \vdots \\ A^{2\to1}_{\mathrm{LoS},k,N_\mathrm{rx}-1}/A^{2\to1}_{\mathrm{LoS},k,0}\cdot \mathrm{e}^{-2\pi\mathrm{j}f_0\left[\tau^{2\to1}_{0,N_\mathrm{rx}-1}-\tau^{2\to1}_{0,0}\right]} \end{bmatrix} + \vec{w}_{\mathrm{awgn},k1}. \tag{27}$$

Due to the normalization with the complex amplitude of the first RX channel, the unknown carrier phases and the phase noise-induced errors cancel each other out. The residual signal's phases depend only on the ToF differences and are distrubed only by the AWGN vector $\vec{w}_{\mathrm{awgn},k1}$. As one target angle per measurement is expected, a subspace-based angle estimation algorithm is used. Thus, the averaged measurement covariance across all chirps is calculated as

$$\underline{S}^{2\to1}_\mathrm{LoS} = \frac{1}{N_\mathrm{ch}}\sum_{k=0}^{N_\mathrm{ch}-1}\vec{x}^{2\to1}_{\mathrm{LoS},k}\vec{x}^{2\to1\,\mathrm{H}}_{\mathrm{LoS},k}, \tag{28}$$

and the multiple signal classification (MUSIC) approach is used for the angle estimation [30]. After an eigenvalue decomposition of $\underline{S}^{2\to1}_\mathrm{LoS}$, the eigenvectors that belong to the $N_\mathrm{RX}-1$ smallest eigenvalues build the noise subspace $\underline{E}_\mathrm{N}$, which is ideally orthogonal to the incident vector of the measurement. The beamformer is then calculated by

$$P_\mathrm{MU}(\alpha) = \frac{1}{\vec{a}^\mathrm{H}(\alpha)\,\underline{E}_\mathrm{N}\underline{E}_\mathrm{N}^\mathrm{H}\vec{a}(\alpha)}, \tag{29}$$

where $\vec{a}(\alpha)$ are the hypotheses of the incident vector. The α that maximizes (29) gives the estimate $\hat{\alpha}$. Analogously, the second angle estimate $\hat{\beta}$ is produced.

B. BASELINE DISTANCE ESTIMATION

As the LoS beat frequencies, from (23) and (24) are disturbed by timing, frequency, and phase noise errors, the round-trip beat frequecies are calculated by adding the estimates for the respective RX channels of the two radars

$$f^\mathrm{RT}_{\mathrm{B,LoS},k,n_\mathrm{A}} = -\mu\left(\tau^{2\to1}_{0,n_\mathrm{A}} + \tau^{1\to2}_{0,n_\mathrm{A}}\right) - 2f_\mathrm{D}, \tag{30}$$

where all synchronization errors are canceled out. This concept has already been used in localization systems, e.g. in [31], where similar processing was applied to eliminate systematic time and frequency errors. To eliminate the Doppler component, the corresponding round-trip phases are also considered, yielding

$$\tilde{\varphi}^\mathrm{RT}_{\mathrm{LoS},k,n_\mathrm{A}} = -2\pi f_0\left[\tau^{2\to1}_{0,n_\mathrm{A}} + \tau^{1\to2}_{0,n_\mathrm{A}} + 2kT_{\mathrm{s,st}}\frac{v_\mathrm{r}}{c_0}\right]. \tag{31}$$

The radial velocity can then be estimated from the slope of the round-trip phases along the slow time — for example, by employing a linear regression approach — and is used to compensate for the Doppler term in (30). The compensated

round-trip frequencies are then proportional to the distances

$$\hat{d}^{\mathrm{RT}}_{n_\mathrm{A}} = -c_0 \cdot \frac{f^{\mathrm{RT}}_{\mathrm{B,LoS},k,n_\mathrm{A}} + 2\hat{f}_\mathrm{D}}{\mu}, \tag{32}$$

where $\hat{f}_\mathrm{D}$ is the estimated Doppler frequency. The round-trip distances for all RX channels can be analytically calculated using the geometric considerations discussed in Section II. The round-trip distances are computed as a function of α and β and the baseline distances d_B for different hypotheses about the latter. The mean over all RX channels of the half round-trip distances serves as good indication of the region of possible hypotheses. A minimum mean square error evaluation of the measurements and hypotheses along the RX channels gives the estimate for the baseline length

$$\hat{d}_\mathrm{B} = \arg\min_{d_\mathrm{B}} \sum_{n_\mathrm{A}=0}^{N_\mathrm{RX}-1} \left| d^{\mathrm{RT}}_{n_\mathrm{A}}\left(d_\mathrm{B}, \hat{\alpha}, \hat{\beta}\right) - \hat{d}^{\mathrm{RT}}_{n_\mathrm{A}} \right|^2. \tag{33}$$

With these three estimates, the relative 2D positions of all antennas are determined. This enables the calculation of all bistatic antenna distances and their corresponding ToFs $\hat{\tau}^{2\to1}_{0,n_\mathrm{A}}$ and $\hat{\tau}^{1\to2}_{0,n_\mathrm{A}}$.

IV. SYNCHRONIZATION

Before the images of the bistatic paths can be generated, disturbances due to time, frequency, and phase errors must be corrected for all samples along the N_ch chirps of a sequence. The LoS link is again crucial for the synchronization steps.

A. FREQUENCY OFFSET

In the correction chain, the estimation of the frequency offset that causes the time drift δ_t is estimated first. The linear drift of the beat frequency (see Section II) is applied to the LoS beat frequency models in (23) and (24). The frequencies are linear functions of the slow time index k with a slope

$$m^{2\to1/1\to2}_{f_\mathrm{B,LoS}} = \pm\mu T_\mathrm{rep}\delta_\mathrm{t}. \tag{34}$$

A linear regression averaged across all RX channels yields an optimal estimate of the slopes in a least square sense given the measured frequencies according to [32]. Fig. 7 shows the measured beat frequencies during one chirp sequence and the residual error after subtracting the linear regression fit. The estimated clock drift is then calculated with the fitted slopes as

$$\hat{\delta}_\mathrm{t} = \frac{\hat{m}^{2\to1}_{f_\mathrm{B}} - \hat{m}^{1\to2}_{f_\mathrm{B}}}{2\mu T_\mathrm{rep}}. \tag{35}$$

With this estimate, the drift-dependent error terms in the signal model obtained from (19) and (20) can be corrected successively. The chirp-dependent frequency shift can be compensated for by a linear phase shift in the time domain. The quadratic fast time phase of $\pm2\pi\mu\delta_\mathrm{t}t^2$, which leads to a loss of resolution [3], is removed by multiplying (21) and (22) with the complex conjugate phasor in the fast time dimension. These steps are combined into a single multiplication applied

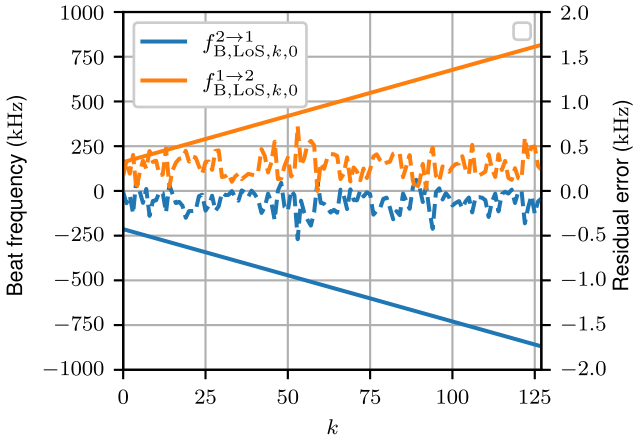

FIGURE 7. Measured LoS beat frequencies for both bistatic radars during one chirp sequence (128 chirps). The dashed lines indicate the residual errors between the measurements and the linear fit. The estimated clock drift amounts to 1.72 ppm.

to the bistatic beat signal for all successive chirps

$$\tilde{s}^{2\to1/1\to2}_{\mathrm{B},k,n_\mathrm{A}}(t) = s^{2\to1/2\to1}_{\mathrm{B},k,n_\mathrm{A}}(t) \cdot \mathrm{e}^{2\pi\mathrm{j}\left[\pm\left(f_{0,\mathrm{c}}\mp\mu k T_\mathrm{rep}\pm\mu t\right)\hat{\delta}_\mathrm{t}t\right]}. \tag{36}$$

This is performed on all additive superimposed parts of the bistatic signal obtained from (21) and (22), thereby correcting the LoS and the image components.

B. TIME OFFSET

The LoS beat frequencies after the previous correction step can be expressed as

$$\tilde{f}^{2\to1}_{\mathrm{B,LoS},k,n_\mathrm{A}} = -\mu\tau^{2\to1}_{0,n_\mathrm{A}} - f_\mathrm{D} + \mu\Delta\tau_0 + \epsilon_{f,\mathrm{pn},k}, \tag{37}$$

$$\tilde{f}^{1\to2}_{\mathrm{B,LoS},k,n_\mathrm{A}} = -\mu\tau^{1\to2}_{0,n_\mathrm{A}} - f_\mathrm{D} - \mu\Delta\tau_0 - \epsilon_{f,\mathrm{pn},k}. \tag{38}$$

The bistatic channels are not reciprocal, as assumed in [18]. Therefore, the bistatic ToFs derived as described in Section III must be compensated for before further processing. The constant frequency offset caused by the initial time offset and the phase noise disturbance can then be estimated as

$$\mu\Delta\hat{\tau}_0 + \hat{\epsilon}_{f,\mathrm{pn},k} \approx \frac{1}{N_\mathrm{RX}} \sum_{n_\mathrm{A}=0}^{N_\mathrm{RX}-1} \frac{\tilde{f}^{2\to1}_{\mathrm{B,LoS},k,n_\mathrm{A}} + \mu\hat{\tau}^{2\to1}_{0,n_\mathrm{A}} - \tilde{f}^{1\to2}_{\mathrm{B,LoS},k,n_\mathrm{A}} + \mu\hat{\tau}^{1\to2}_{0,n_\mathrm{A}}}{2}. \tag{39}$$

Subsequently, this constant shift is compensated for by

$$\tilde{\tilde{s}}^{2\to1/1\to2}_{\mathrm{B},k,n_\mathrm{A}}(t) = \tilde{s}^{2\to1/1\to2}_{\mathrm{B},k,n_\mathrm{A}}(t) \cdot \mathrm{e}^{2\pi\mathrm{j}\left(\mp\mu\Delta\hat{\tau}_0\mp\hat{\epsilon}_{f,\mathrm{pn},k}\right)t}. \tag{40}$$

The operation removes the frequency error due to the time offset $\Delta\tau_0$ and the linear phase part $\epsilon_{f,\mathrm{pn},k}$ of the phase noise $\phi_\mathrm{pn}(t)$ for all targets and the LoS. If the realization of the phase noise for the k-th chirp is expressed as a polynomial series

expansion

$$\phi_{\mathrm{pn},k}(t) \approx \epsilon_{\varphi,\mathrm{pn},k} + \cancel{\epsilon_{f,\mathrm{pn},k} t} + \underbrace{a_2 t^2 + \ldots}_{=\tilde{\phi}_{\mathrm{pn},k}(t)}, \tag{41}$$

there are still a part that contains higher-order polynomials that cause a phase noise skirt, denoted as $\tilde{\phi}_{\mathrm{pn},k}(t)$, and a constant phase error per chirp $\epsilon_{\varphi,\mathrm{pn},k}$ that disturbs the phase coherency across slow time. The correction of the phase noise skirt and the constant phase error is discussed in the following subsections.

C. PHASE NOISE SKIRT

First, the corrected beat signals with all correction steps applied until (40) are written out, yielding (44) and (45), shown at the bottom of the page. In a next step, the beat signals in the frequency domain are shifted, so that the LoS part is located at DC and are normalized with the complex LoS amplitudes $\underline{A}_{\mathrm{LoS}}^{2\to1}$ and $\underline{A}_{\mathrm{LoS}}^{1\to2}$, yielding

$$\tilde{s}_{\mathrm{pn},k}^{2\to1}(t) = \mathrm{e}^{j\tilde{\phi}_{\mathrm{pn},k}(t)} \cdot \left[1 + \sum_{\ell} \underline{a}_{\ell}^{2\to1} \mathrm{e}^{-2\pi \mathrm{j} \Delta f_{\mathrm{B},\ell}^{2\to1} t}\right], \tag{42}$$

$$\tilde{s}_{\mathrm{pn},k}^{1\to2}(t) = \mathrm{e}^{-j\tilde{\phi}_{\mathrm{pn},k}(t)} \cdot \left[1 + \sum_{\ell} \underline{a}_{\ell}^{1\to2} \mathrm{e}^{-2\pi \mathrm{j} \Delta f_{\mathrm{B},\ell}^{1\to2} t}\right], \tag{43}$$

where $\underline{a}_{\ell}^{2\to1/1\to2} = \underline{A}_{\ell}^{2\to1/1\to2} / \underline{A}_{\mathrm{LoS}}^{2\to1/1\to2}$ is the normalized phasor of the image reflection, and $\Delta f_{\mathrm{B},\ell}^{2\to1/1\to2}$ is the beat frequency difference between the ℓ-th image reflection and the corresponding LoS frequency. The quality of the phase noise estimate depends greatly on the relationship between the LoS and the image scatterer amplitudes, which can be seen in Fig. 8. These amplitudes are approximately constant during a single chirp, while their angles rotate proportionally to the beat frequency differences $\Delta f_{\mathrm{B},\ell}^{2\to1/1\to2}$. A worst-case approximation of the resulting phase noise error can be given by the assumption that all normalized image reflections sum up coherently and perpendicularly to the phase noise vector. The maximum possible error in the respective unit's bistatic

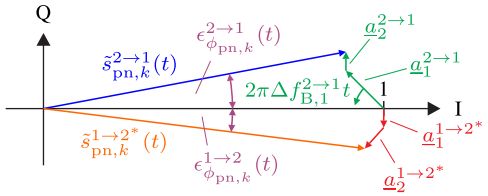

FIGURE 8. Phasor diagram of $\tilde{s}_{\mathrm{pn},k}^{2\to1}(t)$ and $\tilde{s}_{\mathrm{pn},k}^{1\to2^*}(t)$ at a fixed time stamp, which shows the influence of the image reflection on phase noise estimation quality. The in-phase axis aligns with the phase noise value at that time instance.

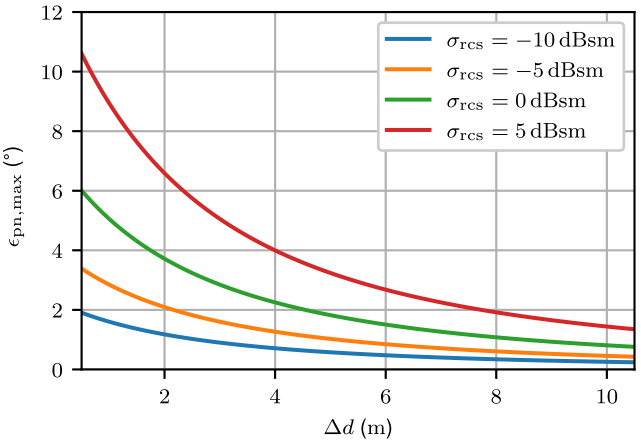

FIGURE 9. Evaluation of the phase estimation error for the phase noise skirt compensation due to a single scatterer in the image. Δd is the difference in distance between the LoS and the image path.

signal is then calculated by

$$\epsilon_{\phi_{\mathrm{pn,max}}}^{2\to1/1\to2} = \arctan\left(\sum_{\ell} \left|\underline{a}_{\ell}^{2\to1/1\to2}\right|\right). \tag{46}$$

This error is evaluated for a single scatterer scenario with different distance offsets between the image path and the LoS and for various RCSs (Fig. 9). In centralized processing, the phase noise estimates for the two stations are averaged to

$$\tilde{\underline{s}}_{\mathrm{B},k,n_{\mathrm{A}}}^{2\to1}(t) = \overbrace{\underline{A}_{\mathrm{LoS}}^{2\to1} \cdot \mathrm{e}^{\mathrm{j}\left(-2\pi f_0\left(\tau_{0,n_{\mathrm{A}}}^{2\to1} + kT_{\mathrm{rep}}\frac{v_{\mathrm{r}}}{c_0}\right) + \Delta\Theta_k + \epsilon_{\varphi,\mathrm{pn},k}\right)}}^{=\underline{A}_{\mathrm{LoS}}^{2\to1}} \cdot \exp\left\{2\pi\mathrm{j}\left[-\mu\tau_{0,n_{\mathrm{A}}}^{2\to1} - f_{\mathrm{D}}\right]t\right\} \cdot \mathrm{e}^{j\tilde{\phi}_{\mathrm{pn},k}(t)}$$
$$+ \sum_{\ell} \underbrace{\underline{A}_{\ell}^{2\to1} \cdot \mathrm{e}^{\mathrm{j}\left(-2\pi f_0\left(\tau_{0,\ell,n_{\mathrm{A}}}^{2\to1} + kT_{\mathrm{rep}}\frac{v_{\mathrm{r},\ell}}{c_0}\right) + \Delta\Theta_k + \epsilon_{\varphi,\mathrm{pn},k}\right)}}_{=\underline{A}_{\ell}^{2\to1}} \cdot \exp\left\{2\pi\mathrm{j}\left[-\mu\tau_{0,\ell,n_{\mathrm{A}}}^{2\to1} - f_{\mathrm{D},\ell}\right]t\right\} \cdot \mathrm{e}^{j\tilde{\phi}_{\mathrm{pn},k}(t)} \tag{44}$$

$$\tilde{\underline{s}}_{\mathrm{B},k,n_{\mathrm{A}}}^{1\to2}(t) = \overbrace{\underline{A}_{\mathrm{LoS}}^{1\to2} \cdot \mathrm{e}^{\mathrm{j}\left(-2\pi f_0\left(\tau_{0,n_{\mathrm{A}}}^{1\to2} + kT_{\mathrm{rep}}\frac{v_{\mathrm{r}}}{c_0}\right) - \Delta\Theta_k - \epsilon_{\varphi,\mathrm{pn},k}\right)}}^{=\underline{A}_{\mathrm{LoS}}^{1\to2}} \cdot \exp\left\{2\pi\mathrm{j}\left[-\mu\tau_{0,n_{\mathrm{A}}}^{1\to2} - f_{\mathrm{D}}\right]t\right\} \cdot \mathrm{e}^{j\tilde{\phi}_{\mathrm{pn},k}(t)}$$
$$+ \sum_{\ell} \underbrace{\underline{A}_{\ell}^{2\to1} \cdot \mathrm{e}^{\mathrm{j}\left(-2\pi f_0\left(\tau_{0,\ell,n_{\mathrm{A}}}^{1\to2} + kT_{\mathrm{rep}}\frac{v_{\mathrm{r},\ell}}{c_0}\right) - \Delta\Theta_k - \epsilon_{\varphi,\mathrm{pn},k}\right)}}_{=\underline{A}_{\ell}^{1\to2}} \cdot \exp\left\{2\pi\mathrm{j}\left[-\mu\tau_{0,\ell,n_{\mathrm{A}}}^{1\to2} - f_{\mathrm{D},\ell}\right]t\right\} \cdot \mathrm{e}^{-j\tilde{\phi}_{\mathrm{pn},k}(t)} \tag{45}$$

reduce the error due to the image signal parts, giving

$$\hat{\tilde{\phi}}_{\mathrm{pn},k}(t) = \frac{\arg\left\{\tilde{s}^{2\to1}_{\mathrm{pn},k}(t)\right\} - \arg\left\{\tilde{s}^{1\to2}_{\mathrm{pn},k}(t)\right\}}{2}. \tag{47}$$

Phase noise skirt compensation is then performed for every chirp in each radar receiver as

$$\tilde{\tilde{s}}^{2\to1/1\to2}_{\mathrm{B},k,n_\mathrm{A}}(t) = \tilde{\tilde{s}}^{2\to1}_{\mathrm{B},k,n_\mathrm{A}}(t)\cdot \mathrm{e}^{\mp\mathrm{j}\hat{\tilde{\phi}}_{\mathrm{pn},k}(t)}. \tag{48}$$

This is simulated in a scenario with one image scatterer with a swept RCS and an additional weak scatterer (Fig. 10) to evaluate the capabilities and limitations of this approach. The results show that even for the strong scatter with an RCS of 5 dBsm, the phase noise skirt, which covers the weak target, is amply compensated for. A similar approach is proposed in [23] to compensate for the phase noise due to a reference link assumed to be considerably stronger than the target reflection. However, the scatterer's influence on performance is not discussed. Our full-duplex approach additionally enables the averaging step in (47), which further improves the estimation, as the phase noise parts are superimposed coherently, while the scatterer phases add up randomly.

D. INITIAL CHIRP PHASES

The last error sources that need to be compensated for fully coherent CS processing are the initial phase differences of the LOs at each chirp $\Delta\Theta_k$ and the additional DC part of the phase noise contribution $\epsilon_{\varphi,\mathrm{pn},k}$. The phases after the skirt compensation are given by

$$\hat{\tilde{\varphi}}^{2\to1}_{\mathrm{LoS},k,n_\mathrm{A}} = -2\pi f_0\left[\tau^{2\to1}_{0,n_\mathrm{A}} + kT_\mathrm{rep}\frac{v_\mathrm{r}}{c_0}\right] + \epsilon_{\varphi,\mathrm{pn},k} + \Delta\Theta_k, \tag{49}$$

$$\hat{\tilde{\varphi}}^{1\to2}_{\mathrm{LoS},k,n_\mathrm{A}} = -2\pi f_0\left[\tau^{1\to2}_{0,n_\mathrm{A}} + kT_\mathrm{rep}\frac{v_\mathrm{r}}{c_0}\right] - \epsilon_{\varphi,\mathrm{pn},k} - \Delta\Theta_k. \tag{50}$$

This chirp-dependent phase offset is calculated in a manner similar to that in [2] by averaging the unwrapped phases across the RX channels as

$$\begin{aligned}\hat{\phi}^{2\to1/1\to2}_k &= \frac{1}{N_\mathrm{rx}}\sum_{n_\mathrm{A}=0}^{N_\mathrm{rx}-1}\mathcal{U}\left(\tilde{\varphi}^{2\to1/1\to2}_{\mathrm{LoS},k,n_\mathrm{A}}\right)\\ &= \phi^{2\to1/1\to2}_0 - 2\pi f_0\, kT_{\mathrm{s,st}}\frac{v_\mathrm{r}}{c_0} \pm \epsilon_{\varphi,\mathrm{pn},k} \pm \Delta\Theta_k,\end{aligned} \tag{51}$$

where $\mathcal{U}(\cdot)$ is the unwrapping operator, and $\phi^{2\to1/1\to2}_0$ is a constant phase term with respect to the chirp index k that depends on the constellation geometry. Here, it is assumed that the phase change due to the radial constant velocity v_r is equal for all RX channels of both radar nodes. The compensation phase for each chirp is calculated by

$$\hat{\phi}_k = \frac{\hat{\phi}^{2\to1}_k - \hat{\phi}^{1\to2}_k}{2} = \phi_0 + \epsilon_{\varphi,\mathrm{pn},k} + \Delta\Theta, \tag{52}$$

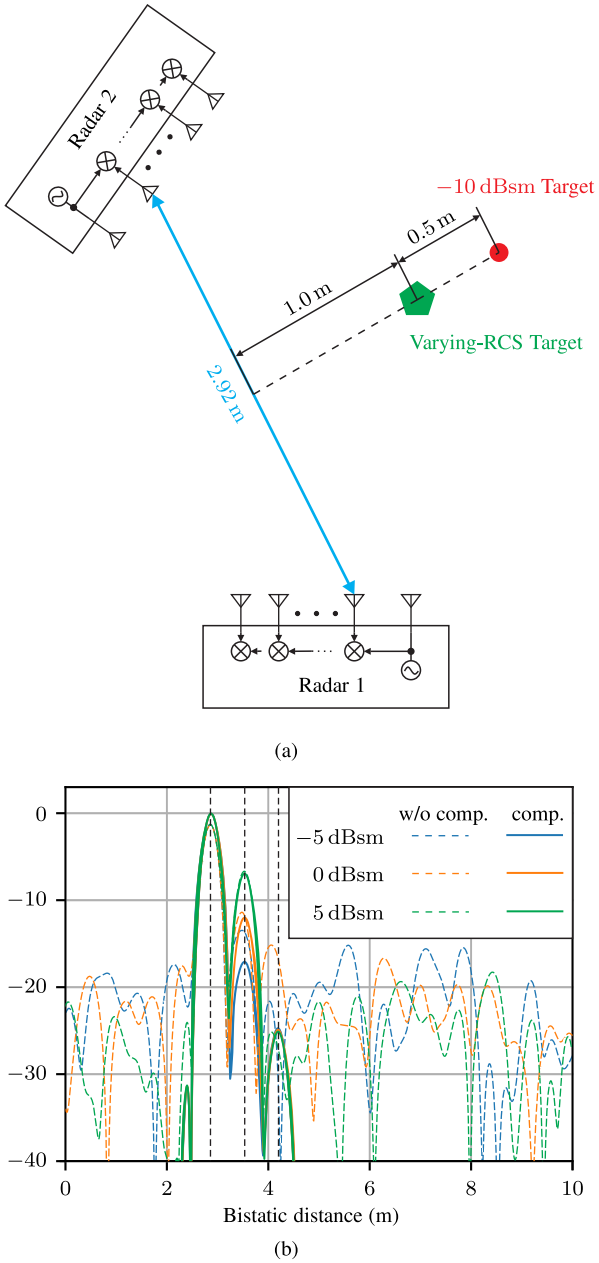

FIGURE 10. Simulation of phase noise skirt compensation performance. (a) Sketch of the image scene with two point scatterers. (b) Range FFTs of the first chirp and the first RX channel of the signal received by radar 2 with (solid lines) and without (dashed lines) skirt compensation.

where ϕ_0 is a residual unknown phase term that is constant for all chirps. Therefore, the compensation step

$$s^{2\to1/1\to2}_{\mathrm{B,coh},k,n_\mathrm{A}}(t) = \mathcal{U}\left\{\tilde{\tilde{s}}^{2\to1}_{\mathrm{B},k,n_\mathrm{A}}(t)\cdot\mathrm{e}^{\mp\mathrm{j}\hat{\phi}_k}\right\} \tag{53}$$

yields the coherent bistatic signals, consisting of a LoS component and the image reflections. The averaging step in (52) reduces the phase ambiguity to π, so π unwrapping along the slow time index must finally be applied to $s^{2\to1/1\to2}_{\mathrm{B,coh},k,n_\mathrm{A}}(t)$. The overall processing chain results are shown in Fig. 11.

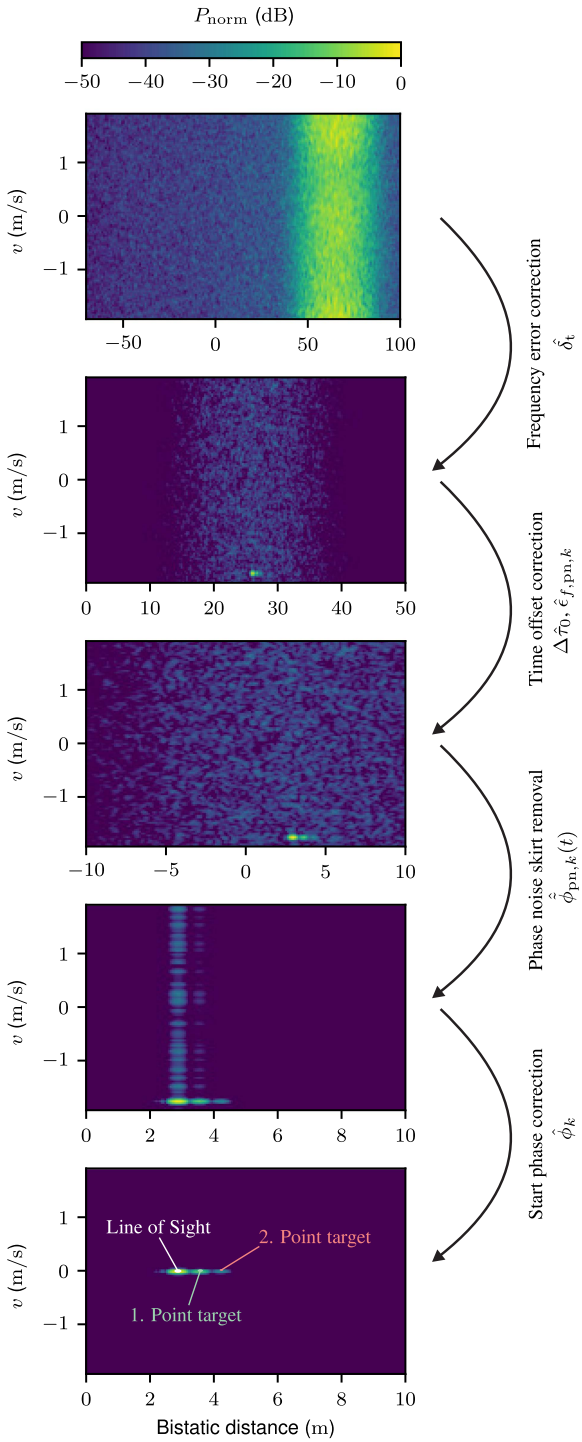

FIGURE 11. Simulated range-Doppler maps of one bistatic channel after the different synchronization steps for the two-target scenario described in Fig. 10(a) for the case of $\sigma_{\mathrm{RCS}} = 0$ dBsm.

V. MULTIPERSPECTIVE IMAGING

After correcting the bistatic signals of both radars, four different images can be generated. A monostatic SIMO image of the 2D scene for each radar node and bistatic images from radar 1 to radar 2 and vice versa are obtained.

A. LINE OF SIGHT REMOVAL

Before image generation, the LoS parts of the bistatic signals are removed using the CLEAN approach, originally intended for radio interferometry [33]. This algorithm can similarly be applied to range-Doppler maps as described in [34]. Only one iteration per RX channel on the coherent bistatic range-Doppler maps is executed, substracting the LoS point spread function (PSF) from the respective map. This prevents weak targets from being obscured by LoS side lobes and minimizes artifacts in the bistatic image.

B. BACK-PROJECTION

The application of the back-projection algorithm has the advantage that all four images can be interpolated on the same xy-grid for further image combination, whereas an azimuth angle FFT-based approach would yield different grids for the two radars. The estimates $\hat{d}_{\mathrm{B}}$, $\hat{\alpha}$, and $\hat{\beta}$ are made as described in Section III. These parameters can be used in conjunction with (12) and (13) estimate the TX and RX antenna positions of the second radar for every chirp $\hat{\vec{p}}_{\mathrm{TX},2,k}$ and $\hat{\vec{p}}_{\mathrm{RX},2,n_{\mathrm{A}},k}$, respectively. In the next step, the algorithm performs the fast time FFTs of all available radar image signals

$$S^{1\to 1/2\to 2}_{\mathrm{B},k,n_{\mathrm{A}}}(f) = \mathcal{F}\left\{s^{1\to 1/2\to 2}_{\mathrm{B},k,n_{\mathrm{A}}}(t)\right\}, \tag{54}$$

$$S^{2\to 1/2\to 2}_{\mathrm{B},k,n_{\mathrm{A}}}(f) = \mathcal{F}\left\{s^{2\to 1/1\to 2}_{\mathrm{B,coh},k,n_{\mathrm{A}}}(t)\right\}, \tag{55}$$

where $s^{1\to 1/2\to 2}_{\mathrm{B},k,n_{\mathrm{A}}}(t)$ are the monostatic beat signals of radars 1 and 2. The image coordinate system is centered on the first RX antenna of radar 1, and the vector from the first RX antenna to the first radar's TX antenna spans the positive x-axis. For every pixel $\vec{p}(x, y)$ in the grid and for all TX–RX constellations in the bistatic scene, the hypothetical distance is calculated as

$$d^{i\to j}_{\mathrm{hyp},k,n_{\mathrm{A}}}(x,y) = \left\|\vec{p}(x,y) - \vec{p}_{\mathrm{TX},i,k}\right\| + \left\|\vec{p}_{\mathrm{RX},j,n_{\mathrm{A}},k} - \vec{p}(x,y)\right\|, \tag{56}$$

where $i, j \in \{1, 2\}$ is the index of the transmitting and receiving radars. Then, the respective spectrum $S^{i\to j}_{\mathrm{B},k,n_{\mathrm{A}}}(f)$ is interpolated linearly in phase and amplitude at the beat frequency

$$f^{i\to j}_{\mathrm{B}}(x,y) = -\mu\frac{d^{i\to j}_{\mathrm{hyp},k,n_{\mathrm{A}}}(x,y)}{c_0} \tag{57}$$

that belongs to the corresponding pixel. The final image can be calculated by

$$I^{i\to j}_{\mathrm{img}}(x,y) = \sum_{n_{\mathrm{A}}=0}^{N_{\mathrm{RX}}-1}\sum_{k=0}^{N_{\mathrm{ch}}-1} S^{i\to j}_{\mathrm{B},k,n_{\mathrm{A}}}\left(f^{i\to j}_{\mathrm{B}}(x,y)\right)\cdot \mathrm{e}^{2\pi \mathrm{j} f_{\mathrm{c}}\frac{d^{i\to j}_{\mathrm{hyp},k,n_{\mathrm{A}}}(x,y)}{c_0}}, \tag{58}$$

where $f_{\mathrm{c}} = f_0 + B/2$ is the chirp's center frequency. The frequency offset in the MHz range due to FDM can be ignored. A real-time implementation of the described algorithm can be found in [35].

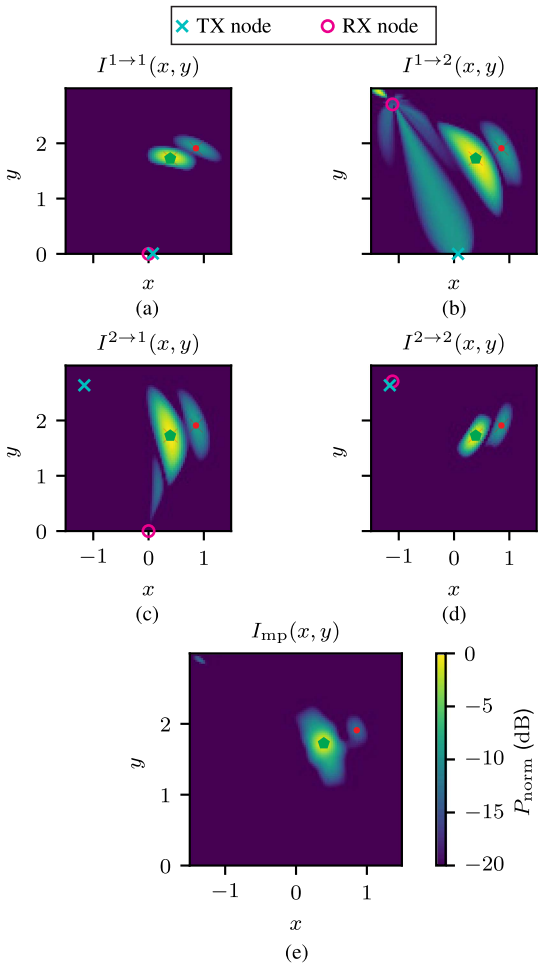

FIGURE 12. Simulated radar images of the scene described in Fig. 9 with target RCSs of 0 dBsm and −10 dBsm. The images for each TX–RX constellation are (a) monostatic radar 1, (b) bistatic 1 → 2, (c) bistatic 2 → 1, (d) monostatic radar 2, and (e) combined multiperspective image.

C. IMAGE COMBINATION

The coherent superposition of all images would result in an interferogram with a geometry-dependent PSF of all image scatterer. As the radars are widely separated in terms of the carrier wavelength $\lambda_0 = \frac{c_0}{f_0}$, these PSFs would show significant side lobes which would complicate the image interpretation [36]. Instead, the magnitudes of all single coherent images, the two monostatic ones and the two bistatic ones, are summed up to generate the final multiperspective image:

$$I_{\mathrm{img,mp}}(x,y) = \sum_{i=0}^{1}\sum_{j=0}^{1}\left|I_{\mathrm{img}}^{i\to j}(x,y)\right|. \tag{59}$$

There are processing techniques that enable super-resolution imaging through fully coherent fusion with large sparse arrays, such as the neural network approach described in [37]. However, such techniques are beyond the scope of this work. The results of the proposed image processing method are shown in Fig. 12, with two point scatterers placed in the image scene. As the simulation model does not cover complex scattering effects, the benefits of this multiperspective imaging are demonstrated through various real radar measurements, which are described in Section VI.

TABLE 1. Radar Parameters

Symbol	Quantity	Value
B	Bandwidth	1.5 GHz
N_{RX}	RX channels	16
T_{ch}	Chirp duration	512 µs
T_{rep}	Chirp repetition time	1024 µs
f_0	Carrier frequency	76 GHz
Δf	Offset frequency	2 MHz
f_{s}	Sampling rate	8 MHz
N_{cs}	Chirps per sequence	128

VI. MEASUREMENT VERIFICATION

To prove the proposed concept, a measurement setup with two 77 GHz FMCW SIMO radar nodes, each equipped with 16 RX antennas with $\lambda/2$ spacing is created. The setup is depicted in Fig. 13, with three different target scenes. Table 1 displays the signal parameters used in the measurement. The radars have an external trigger input, which is used to coarsely align the start times of the chirp sequences. The work presented in [38] is well suited for the pre-synchronization, achieving a time accuracy of a few nanoseconds. To simplify the setup, an arbitrary waveform generator is used as a common trigger source. The resulting initial time offset $\Delta\tau_0$ is in the range of a few hundred nanoseconds due to unknown delays in the trigger signal distribution. One radar node is mounted on a linear rail to vary the constellation in a static measurement. Optical markers are attached to the radar nodes and the to the targets to track their positions and orientations with an optical reference system. The reference system's 3D marker position accuracy is about 1 mm.

A. CONSTELLATION ESTIMATION ACCURACY

To evaluate the localization performance regarding the 2D pose of the second radar relative to the first one, the localization parameters α, β, and d_{B}, which fully describe the relative 2D pose, are estimated. The second radar is moved to different positions on the linear rail. At each of those positions, 20 chirp sequence measurements are performed for five different target scenes, yielding a total of 100 measurements per position. The kind of target (single cylinder, single rod, multiple cylinders, front-looking mannequin, side-looking mannequin) does not influence the localization result, whereas the second radar's position does. The different constellations and error statistics are shown in Table 2. The resulting errors compared to the optical reference system are plotted in histograms in Fig. 14. Two points are noteworthy. First, the angle measurements of

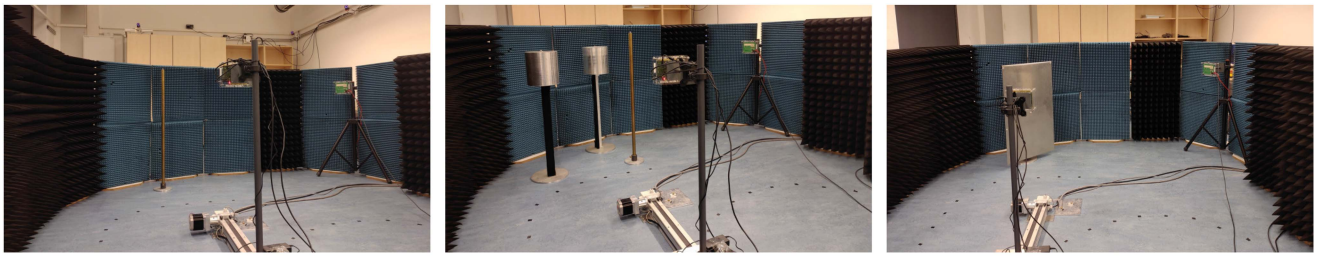

(a) (b) (c)

FIGURE 13. Measurement setup for the verification of the proposed constellation estimation and multiperspective imaging approach. (a) Scene with a small metal rod. (b) Scene with two large cylinders and a small metal rod. (c) Scene with a tilted metal plate.

TABLE 2. Self-Localization Performance Results for Different Radar Constellations Expressed as Means and Standard Deviation of the Localization Parameters

Constellation			Localization accuracy					
α	β	d_B	$\mu_{\Delta\alpha}$	$\sigma_{\Delta\alpha}$	$\mu_{\Delta\beta}$	$\sigma_{\Delta\beta}$	$\mu_{\Delta d_\mathrm{B}}$	$\sigma_{\Delta d_\mathrm{B}}$
18.4°	−36.4°	2.71 m	1.1°	0.1°	1.8°	0.3°	1.0 cm	0.1 cm
15.2°	−39.8°	2.51 m	1.7°	0.1°	2.2°	0.3°	3.5 cm	0.1 cm
11.4°	−43.6°	2.32 m	1.3°	0.1°	1.0°	0.2°	5.5 cm	0.4 cm
6.9°	−48.1°	2.14 m	1.7°	0.1°	2.4°	0.2°	4.9 cm	0.6 cm

both radars (α and β) exhibit an offset that slightly depends on the relative position. A possible explanation is inadequate RX array calibration that does not incorporate effects such as mutual coupling [39]. Second, the distance offset varies greatly with different positions of the moving radar. Furthermore, the spread of the error distribution increases with greater offset. Varying multipath conditions, which are given for different constellations, can lead to different biases and standard deviations for the bistatic ranging results, as demonstrated in [40].

B. TARGET LOCALIZATION PERFORMANCE

To determine the system's localization accuracy, measurements with a metal rod, shown in Fig. 13(a), are performed. The rod's diameter is 3.0 cm, so the rod can be approximately regarded as a point target in the 2D scene. The localization results are shown in Fig. 15. As the constellation estimation error of the second radar node influences the target localization, the measurements that incorporate radar node 2 vary slightly. Nevertheless, the mean errors of the combined image are 0.49 cm in x and −1.68 cm in y, with standard deviations of 0.37 cm and 0.39 cm, respectively. This shows good target localization accuracy for all coherent images and their combination.

C. IMAGING OF TARGETS WITH DIFFERENT SCATTERING CHARACTERISTICS

Section IV presents simulations performed to assess phase noise skirt compensation in the presence of targets with

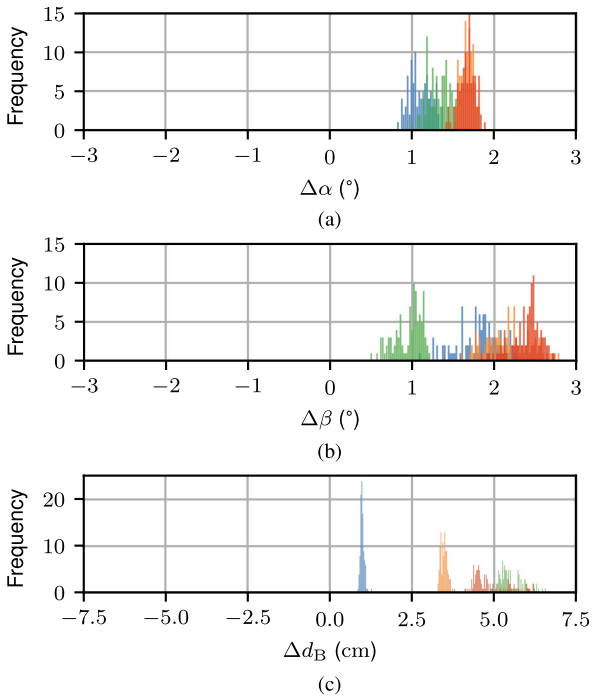

FIGURE 14. Histogram of the measurement errors for the incident angles (a) α, (b) β, and (c) the baseline distance d_B shown in Table 2. Blue: first row; orange second row; green: third row; and red: fourth row of Table 2.

different RCSs. To verify the simulation results, bistatic measurements with a small metal rod as weak target and two aluminum cylinders with high RCSs are conducted, as shown in Fig. 13(b). The results shown in Fig. 16 indicate that the phase noise skirt is significantly reduced. Hence, the weak metal rod reflection can be resolved in the range FFT after phase noise skirt compensation. Fig. 17 shows a range-Doppler map of the bistatic signal transmitted from radar 2 to the first RX channel of radar 1 providing a comparison of the synchronization measurement results with the simulation results. The map after synchronization is clearly focused in the range and azimuth axes, and the LoS signal and the target reflections can be seen. Fig. 18 shows the back-projection results of the bistatic and each monostatic signal combined in an RGB image, demonstrating the system's multiperspective

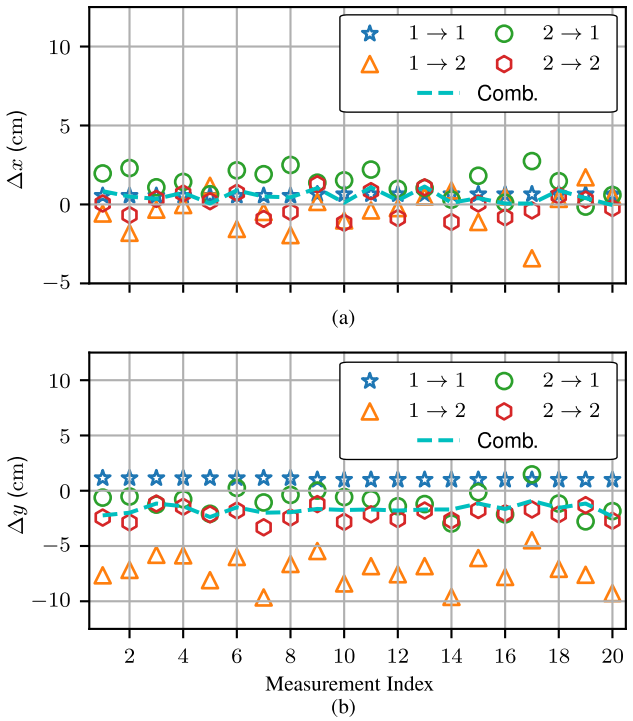

FIGURE 15. Localization errors in the (a) *x* and (b) *y* dimensions over 20 measurements of the metal rod scene shown in Fig. 13(a). The bistatic constellation is the one shown in the first row of Table 2. Each plot shows the results for different monostatic and bistatic combinations as well as the combined results.

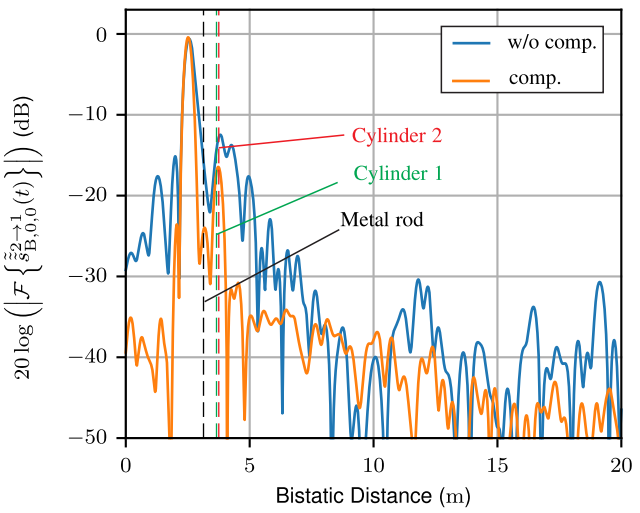

FIGURE 16. Measured bistatic signal from radar 2 to radar 1 before and after the compensation step in (48). The corresponding measurement scene is depicted in Fig. 13(b).

imaging capability in this measurement scenario. The multiperspective approach provides additional information about the geometry of the targets, as different scattering points on the surface of the geometrically extended cylinders are visible in the different images' paths.

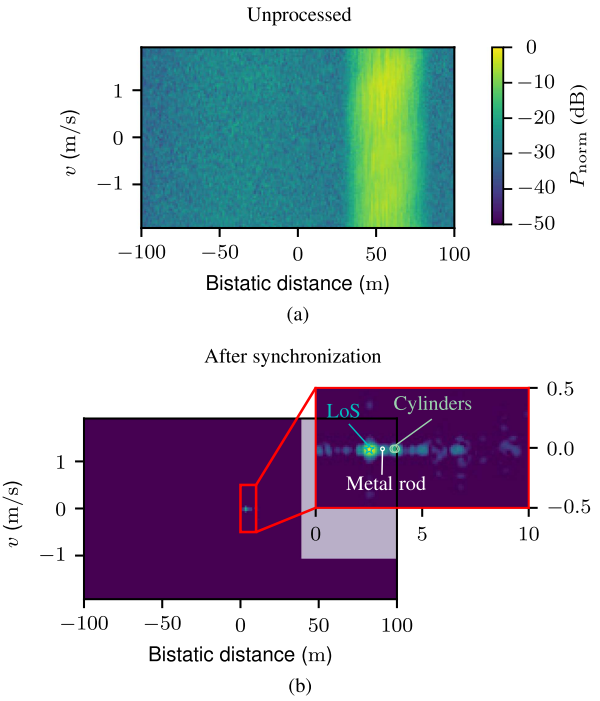

FIGURE 17. Comparison of bistatic range-Doppler maps (a) before and (b) after synchronization processing. The corresponding measurement scene is shown in Fig. 13(b).

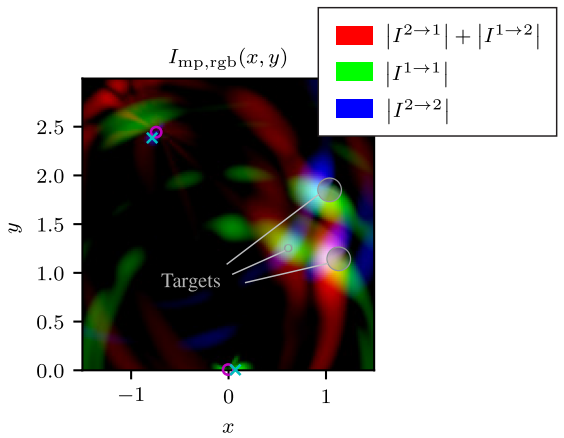

FIGURE 18. Combination of a bistatic image (red), a monostatic image from radar 1 (green) and a monostatic image from radar 2 (blue) into one RGB image with an image depth of 20 dB.

As mentioned earlier, a major advantage of bistatic imaging with widely separated nodes is the detection of targets with highly angle-dependent RCSs. As an example for such a target, the scattering characteristics in the monostatic case for a metal plate can be mathematically derived using the physical optics approximation presented in [41]:

$$\sigma_{\mathrm{PO}}(\theta) = \frac{4\pi a^2 b^2}{\lambda^2} \cos^2(\theta) \left(\frac{\sin(ka \sin\theta)}{ka \sin\theta} \right)^2, \qquad (60)$$

where a and b are the dimensions of the plate, and θ, k, and λ are the incident angle of the electromagnetic wave, the wave number, and the wavelength, respectively. The $\cos^2(\theta)$

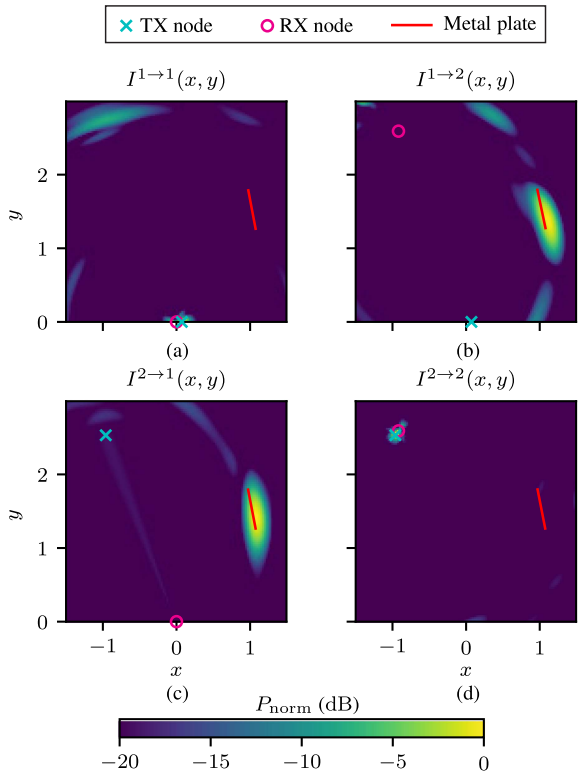

FIGURE 19. Radar images of the scene with a tilted metal plate shown in 13(c): (a) monostatic radar 1, (b) bistatic 1 → 2, (c) bistatic 2 → 1, and (d) monostatic radar 2.

function causes a decreasing envelope for a tilt of the plate with respect to the direction of arrival. To demonstrate this effect, bistatic radar measurements are performed with a tilted metal plate, shown in Fig. 13(c). The resulting radar images for all TX–RX combinations are illustrated in Fig. 19. All pixel values are normalized to the maximum in the respective image. For the monostatic images, TX–RX coupling produces the highest peak, while the metal plate is not visible. In constrast, as expected, the tilted plate produces a strong reflection in the bistatic images.

VII. CONCLUSION AND FUTURE WORK

This paper presents a comprehensive signal model for uncoupled bistatic radar network that incorporates time and frequency offsets as well as distortions due to uncorrelated phase noise. Based on this model, a complex algorithm is proposed that can estimate the relative 2D pose of the involved radar nodes and compensates for the time, frequency, and phase errors in the bistatic beat signal to enable coherent range-Doppler processing. The algorithm finally generates a multiperspective radar image by superimposing the different coherent monostatic and bistatic images. These processing steps are validated through real bistatic radar measurements, showing a localization accuracy of a few centimeters and demonstrating the advantages of bistatic and multiperspective imaging in the presence of complex targets. As we have demonstrated the capabilities of coherent signal processing in a bistatic uncoupled cooperative radar network for artificial target scenes, future work will focus on multiperspective imaging for real use cases, such as automotive applications and radar remote sensing. For the related measurements, narrowband communication systems, such as those presented in [38] and [42], will be integrated to achieve wireless pre-synchronization in the nanosecond range for time synchronicity and frequency accuracy on a scale of parts per billion and to transfer moderate amounts of data for online processing.

REFERENCES

[1] C. Waldschmidt, J. Hasch, and W. Menzel, "Automotive radar–from first efforts to future systems," *IEEE J. Microwaves*, vol. 1, no. 1, pp. 135–148, Jan. 2021.
[2] M. Gottinger, P. Gulden, and M. Vossiek, "Coherent signal processing for loosely coupled bistatic radar," *IEEE Trans. Aerosp. Electron. Syst.*, vol. 57, no. 3, pp. 1855–1871, Jun. 2021.
[3] V. Janoudi, P. Schoeder, T. Grebner, N. Appenrodt, J. Dickmann, and C. Waldschmidt, "Signal model for coherent processing of uncoupled and low frequency coupled MIMO radar networks," *IEEE J. Microwaves*, vol. 4, no. 1, pp. 69–85, Jan. 2024.
[4] D. Werbunat et al., "Multichannel repeater for coherent radar networks enabling high-resolution radar imaging," *IEEE Trans. Microw. Theory Techn.*, early access, Nov. 30, 2023, doi: 10.1109/TMTT.2023.3326284.
[5] L. Leyva, D. Castanheira, A. Silva, A. Gameiro, and L. Hanzo, "Cooperative multiterminal radar and communication: A new paradigm for 6G mobile networks," *IEEE Veh. Technol. Mag.*, vol. 16, no. 4, pp. 38–47, Dec. 2021.
[6] A. Guerra, D. Dardari, and P. M. Djuric, "Dynamic radar networks of UAVs: A tutorial overview and tracking performance comparison with terrestrial radar networks," *IEEE Veh. Technol. Mag.*, vol. 15, no. 2, pp. 113–120, Jun. 2020.
[7] B. Hawkins, M. Anderson, S. Prager, S.-I. Chung, and M. Lavalle, "Experiments with small UAS to support SAR tomographic mission formulation," in *Proc. IEEE Int. Geosci. Remote Sens. Symp.*, 2021, pp. 643–646.
[8] F. Santi, M. Antoniou, and D. Pastina, "Point spread function analysis for GNSS-based multistatic SAR," *IEEE Geosci. Remote Sens. Lett.*, vol. 12, no. 2, pp. 304–308, Feb. 2015.
[9] S. Brisken, "Multistatic ISAR - Chances and challenges," in *Proc. Int. Radar Conf.*, 2014, pp. 1–6.
[10] B. Griffin, A. Balleri, C. Baker, and M. Jahangir, "Optimal receiver placement in staring cooperative radar networks for detection of drones," in *Proc. IEEE Radar Conf.*, 2020, pp. 1–6.
[11] K. L. Bell, J. T. Johnson, C. J. Baker, G. E. Smith, and M. Rangaswamy, "Modeling and simulation for multistatic coherent MIMO radar," in *Proc. IEEE Radar Conf.*, 2013, pp. 1–6.
[12] M. I. Skolnik, Ed., *Radar Handbook*, 2nd ed. New York, NY, USA: McGraw-Hill, 1990.
[13] H. Griffiths, "From a different perspective: Principles, practice and potential of bistatic radar," in *Proc. Int. Conf. Radar*, 2003, pp. 1–7.
[14] B. Griffin, A. Balleri, C. Baker, and M. Jahangir, "Prototyping a dual-channel receiver for use in a staring cooperative radar network for the detection of drones," in *Proc. 21st Int. Radar Symp.*, 2021, pp. 1–7.
[15] R. J. Burkholder, I. J. Gupta, and J. T. Johnson, "Comparison of monostatic and bistatic radar images," *IEEE Antennas Propag. Mag.*, vol. 45, no. 3, pp. 41–50, Jun. 2003.
[16] Y. Yang and R. S. Blum, "Phase synchronization for coherent MIMO radar: Algorithms and their analysis," *IEEE Trans. Signal Process.*, vol. 59, no. 11, pp. 5538–5557, Nov. 2011.
[17] M. Schartel, R. Bahnemann, R. Burr, W. Mayer, and C. Waldschmidt, "Position acquisition for a multicopter-based synthetic aperture radar," in *Proc. IEEE 20th Int. Radar Symp.*, 2019, pp. 1–7.
[18] M. Gottinger, F. Kirsch, P. Gulden, and M. Vossiek, "Coherent full-duplex double-sided two-way ranging and velocity measurement between separate incoherent radio units," *IEEE Trans. Microw. Theory Techn.*, vol. 67, no. 5, pp. 2045–2061, May 2019.

[19] M. Gottinger et al., "Coherent automotive radar networks: The next generation of radar-based imaging and mapping," *IEEE J. Microwaves*, vol. 1, no. 1, pp. 149–163, Jan., 2021.
[20] A. Frischen, J. Hasch, and C. Waldschmidt, "A cooperative MIMO radar network using highly integrated FMCW radar sensors," *IEEE Trans. Microw. Theory Techn.*, vol. 65, no. 4, pp. 1355–1366, Apr. 2017.
[21] A. Frischen, G. Hakobyan, and C. Waldschmidt, "Coherent measurements with MIMO radar networks of incoherent FMCW sensor nodes," *IEEE Microw. Wireless Compon. Lett.*, vol. 30, no. 7, pp. 721–724, Jul. 2020.
[22] M. Bauduin and A. Bourdoux, "Impact of phase noise on FMCW and PMCW radars," in *Proc. IEEE Rad. Conf.*, 2023, pp. 1–6.
[23] D. Werbunat et al., "On the synchronization of uncoupled multistatic PMCW radars," *IEEE Trans. Microw. Theory Techn.*, early access, Feb. 07, 2024, doi: 10.1109/TMTT.2024.3359035.
[24] A. Grathwohl, B. Meinecke, M. Widmann, J. Kanz, and C. Waldschmidt, "UAV-based bistatic SAR-imaging using a stationary repeater," *IEEE J. Microwaves*, vol. 3, no. 2, pp. 625–634, Apr. 2023.
[25] A. Sakhnini, A. Bourdoux, and S. Pollin, "Estimation of array locations, orientations, timing offsets and target locations in bistatic radars," *IEEE Trans. Radar Syst.*, vol. 1, pp. 520–531, 2023.
[26] P. Tschapek, G. Korner, P. Fenske, C. Carlowitz, and M. Vossiek, "A novel approach for modeling and digital generation of RF signals distorted by bandlimited phase noise," *IEEE J. Microwaves*, vol. 2, no. 4, pp. 699–710, Oct. 2022.
[27] M. Born, E. Wolf, and P. Knight, *Principles of Optics*, 7th ed. Cambridge, U.K.: Cambridge Univ. Press, 2019.
[28] J. J. M. de Wit, W. L. van Rossum, and A. J. de Jong, "Orthogonal waveforms for FMCW MIMO radar," in *Proc. IEEE RadarCon*, 2011, pp. 686–691.
[29] L. Piotrowsky, T. Jaeschke, S. Kueppers, J. Siska, and N. Pohl, "Enabling high accuracy distance measurements with FMCW radar sensors," *IEEE Trans. Microw. Theory Techn.*, vol. 67, no. 12, pp. 1–12, Dec. 2019.
[30] R. Schmidt, "Multiple emitter location and signal parameter estimation," *IEEE Trans. Antennas Propag.*, vol. AP-34, no. 3, pp. 276–280, 1986.
[31] W. Scheiblhofer, S. Scheiblhofer, J. O. Schrattenecker, S. Vogl, and A. Stelzer, "A high-precision long range cooperative radar system for rail crane distance measurement," in *Proc. IEEE 11th Eur. Radar Conf.*, 2014, pp. 305–308.
[32] P. J. Martin, *Linear Regression: An Introduction to Statistical Models*. London, U.K.: SAGE, 2021.
[33] J. Högbom, "Aperture synthesis with a non-regular distribution of interferometer baselines," *Astron. Astrophys. Suppl.*, vol. 15, 1974, Art. no. 417.
[34] T. Wagner, R. Feger, and A. Stelzer, "Cluster CLEAN: An application of CLEAN to LFMCW radar systems," in *Proc. IEEE 11th Eur. Radar Conf.*, 2014, pp. 173–176.
[35] M. Hoffmann et al.,, "Implementation of real-time automotive SAR imaging," in *Proc. IEEE 20th Eur. Radar Conf.*, 2023, pp. 327–330.
[36] N. A. Goodman and J. M. Stiles, "Resolution and synthetic aperture characterization of sparse radar arrays," *IEEE Trans. Aerosp. Electron. Syst.*, vol. 39, no. 3, pp. 921–935, Jul. 2003.
[37] C. Schuessler, M. Hoffmann, and M. Vossiek, "Super-resolution radar imaging with sparse arrays using a deep neural network trained with enhanced virtual data," *IEEE J. Microwaves*, vol. 3, no. 3, pp. 980–993, Jul. 2023.
[38] R. Ghasemi, T. Koegel, P. Fenske, R. Schober, and M. Vossiek, "Time and frequency synchronization for real-time wireless digital communication systems," in *Proc. IEEE 15th German Microw. Conf.*, 2024, pp. 13–16.
[39] E. Sippel, M. Lipka, J. Geib, M. Hehn, and M. Vossiek, "In-situ calibration of antenna arrays within wireless locating systems," *IEEE Trans. Antennas Propag.*, vol. 68, no. 4, pp. 2832–2841, Apr. 2020.
[40] R. Feger, C. Pfeffer, W. Scheiblhofer, C. M. Schmid, M. J. Lang, and A. Stelzer, "A 77-GHz cooperative radar system based on multi-channel FMCW stations for local positioning applications," *IEEE Trans. Microw. Theory Techn.*, vol. 61, no. 1, pp. 676–684, Jan. 2013.
[41] B. R. Mahafza, *Radar Systems Analysis and Design Using MATLAB*, 4th ed. Boca Raton, FL, USA: CRC Press, 2022.
[42] F. Kirsch and M. Vossiek, "Distributed Kalman filter for precise and robust clock synchronization in wireless networks," in *Proc. IEEE Radio Wireless Symp.*, 2009, pp. 482–485.

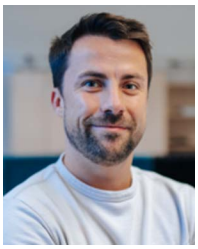

PATRICK FENSKE (Graduate Student Member, IEEE) received the B.Sc. and M.Sc. degrees in electrical engineering from Friedrich-Alexander-Universität Erlangen-Nürnberg (FAU), Erlangen, Germany, in 2019, where he is currently working toward the Ph.D. degree. In 2019, he joined the Institute of Microwaves and Photonics (LHFT), FAU. His research interests include radar system design and signal processing techniques in the field of synchronization and localization of multistatic radar networks.

TOBIAS KOEGEL (Graduate Student Member, IEEE) was born in Lauf, Germany, in 1995. He received the M.Sc. degree in electrical engineering from Friedrich-Alexander-Universität Erlangen-Nürnberg, Erlangen, Germany, in 2020, where he is currently working toward the Ph.D. degree with the Institute of Microwaves and Photonics. His research interest focuses on localization systems based on software defined radios for distributed 6G radar communication networks.

ROGHAYEH GHASEMI (Graduate Student Member, IEEE) received the M.Sc. degree in electrical engineering-optical integrated circuits from the University of Tabriz, Tabriz, Iran. Since 2022, she has been a Research Assistant with the Institute of Microwaves and Photonics (LHFT), Friedrich-Alexander-Universität Erlangen-Nürnberg (FAU), Erlangen. Her research interests focuses on investigating advanced synchronization concepts for multi-static phase-coherent localization networks.

MARTIN VOSSIEK (Fellow, IEEE) received the Ph.D. degree from Ruhr-Universität Bochum, Bochum, Germany, in 1996. In 1996, he joined Siemens Corporate Technology, Munich, Germany, where he was the Head of the Microwave Systems Group from 2000 to 2003. Since 2003, he has been a Full Professor with Clausthal University, Clausthal-Zellerfeld, Germany. Since 2011, he has been the Chair of the Institute of Microwaves and Photonics (LHFT), Friedrich-Alexander-Universität Erlangen-Nürnberg, Erlangen, Germany. He has authored or coauthored more than 400 publications. His research has led to more than 100 granted patents. His research interests include radar, microwave systems, wave-based imaging, transponders, RF identification, communications, and wireless sensor and locating systems. He is the spokesman of the Collaborative Research Centre (CRC 1483) EmpkinS, where more than 80 researchers aim to develop innovative wireless and wave-based sensor technologies for medicine and psychology. He is a member of the German National Academy of Science and Engineering (acatech) and German Research Foundation's (DFG) Review Board. He is a member of the IEEE Microwave Theory and Technology (MTT) Technical Committees for MTT-24 Microwave/mm-Wave Radar, Sensing, and Array Systems, MTT-27 Connected and Autonomous Systems (as founding chair), and MTT-29 Microwave Aerospace Systems. He also serves on the advisory board of the IEEE CRFID Technical Committee on Motion Capture & Localization. He was the recipient of numerous best paper prizes and other awards. He was also the recipient of the Microwave Application Award by the IEEE MTT Society (MTT-S) for Pioneering Research in Wireless Local Positioning Systems in 2019. He has been a member of organizing committees and technical program committees for many international conferences and has served on the review boards of numerous technical journals. From 2013 to 2019, he was an Associate Editor for IEEE TRANSACTIONS ON MICROWAVE THEORY AND TECHNIQUES. Since 2022, he has been an Associate Editor-in-Chief for IEEE TRANSACTIONS ON RADAR SYSTEMS.